How does salinity shape ocean circulation and ice geometry on Enceladus and other icy satellites?

Wanying Kang[1*], Tushar Mittal [1], Suyash Bire [1], Jean-Michel Campin [1], John Marshall [1]
[1]Earth, Atmospheric and Planetary Science Department, Massachusetts Institute of Technology
77 Massachusetts Ave., MA02139, USA
* E-mail: wanying@mit.edu

Of profound astrobiological interest, Enceladus appears to have a global saline subsurface ocean, indicating water-rock reaction at present or in the past, an important mechanism in the moon's potential habitability. Here, we investigate how salinity and the partition of heat production between the silicate core and the ice shell affect ocean dynamics and the associated heat transport – a key factor determining equilibrium ice shell geometry. Assuming steady state conditions, we show that the meridional overturning circulation of the ocean, driven by heat and salt exchange with the poleward-thinning ice shell, has opposing signs at very low and very high salinities. Regardless of these differing circulations, heat and freshwater converge towards the equator, where the ice is thick, acting to homogenize thickness variations. In order to maintain the observed ice thickness variation, the polar-amplified ice dissipation needs to be large enough and ocean heat convergence small enough that it does not overwhelm well-constrained heat loss rates through the thick equatorial ice sheet. This requirement is found to be violated if the main heat source is in the core rather than the ice shell, or if the ocean is very fresh or very salty. Instead, with

a salinity of intermediate range, the temperature- and salinity-induced density gradient largely cancel one another, leading to much reduced overturning and equatorial heat convergence rates, so that the observed ice topography can be sustained.

1 Introduction

Since the Cassini and Galileo missions, Enceladus (a satellite of Saturn) and Europa (a satellite of Jupiter) have been revealed to have high astrobiological potential, satisfying all three necessary conditions for life: 1) the presence of liquid water (*1, 2*), 2) a source of energy (*3, 4*), and 3) a suitable mix of chemical elements (*1, 5–10*). In particular, the geyser-like sprays ejected from the fissures over Enceladus's south pole (*11–13*) provide a unique opportunity to understand the chemistry and dynamics of Enceladus' interior without landing on and drilling through a typically 20km-thick ice shell (*14–18*). Within the geyser samples collected by Cassini, CO_2, methane (*5*), sodium salt (*1*), hydrogen (*7*), and macromolecular organic compounds (*8*) have been found. This suggests a chemically active environment that could sustain life (*9, 10*). However, to infer the chemical environment of the subsurface ocean using plume samples, one needs to better understand the ocean circulation, which governs the transport of chemical tracers. This is the main goal of the present study.

Ocean circulation on Enceladus is driven by heat and salinity fluxes from the core (*3*) and the ice shell (*4, 19, 20*), as well as mechanical forcing, such as tides and libration (*21, 22*). The partition of heat production between the ice and the core has a direct control over ocean dynamics. Moreover, ocean salinity plays a key role since it determines whether density decreases or increases with temperature (*24*) (see Fig.1c). For example, if the ocean is very fresh then heat released by hydrothermal vents will not trigger penetrative convection from below (*25*). Furthermore, the global scale circulation of a salty ocean could be completely different from that of a fresh ocean, as has been explored in Earth's ocean and terrestrial exoplanets (*26, 27*).

Despite its importance, the heat partition is poorly constrained due to our limited understanding of the rheology of both the ice shell and the silicate core. Hydrogen and nanometre-sized silica particles have been detected on Enceladus, providing clear geochemical evidence for active seafloor venting (*6, 7*). However, whether this submarine hydrothermalism, powered by tidal dissipation (*3*), is the dominant heat source preventing the ocean from freezing remains inconclusive due to our limited understanding of the core's rheology (*3, 28*). Another potential heat source is tidal dissipation within the ice shell itself. While poleward-thinning ice geometry on top of the ocean is qualitatively consistent with heating primarily occurring in the ice shell (*18*), present dynamical models of ice are unable to reproduce enough heat to maintain such a thin ice shell (*4, 29*). Attempts to account for higher heat generation through use of more advanced models of ice rheology have thus far not been successful (*4, 19, 29–33*).

An additional complication is that the salinity of Enceladus' ocean remains uncertain. Calculations of thermochemical equilibria over a range of hydrothermal and freezing conditions for chondritic compositions, suggest a salinity ranging between 2-20 psu (g/kg), with a high likelihood of it being below 10 psu (*34–36*). However, at least 17 psu is required to keep the liquid-gas interface of the south polar geysers convectively active enough to ensure that they do not freeze up (*37*). Sodium-enriched samples taken from south pole sprays by Cassini have a salinity of 5-20 psu. This can be considered a lower bound since the interaction of cold water vapor sprays with their environment is likely to lower the salinity of droplets through condensation (*1*). This is also uncertain, however, since fractional crystallization and disequilibrium chemistry may partition components in such a way that geyser particles are not directly representative of the underlying ocean (*38*). Furthermore, if particles originate from a hydrothermal vent, composition can also deviate far from that of the overall ocean (*3, 36*). In a separate line of argument, the size of silica nano-particles carried along in the sprays suggests a salinity

< 40 psu, but this is sensitive to assumptions about ocean pH and the dynamics of hydrothermal vents (*6*).

Given the uncertainties associated with the ocean salinity and heat partition, it is crucial to consider different possible scenarios. Once we understand how ocean circulation and heat transport vary with these variables, we may be able to put further constraints on them, because ocean heat transport can shape the ice shell in geological timescale and the observed ice geometry should not be too far from equilibrium.

Drivers of ocean circulation on Enceladus Data provided by Cassini has enabled reconstructions to be made of Enceladus' ice thickness variations (*14–18*). The solid curve in Fig.1b shows the zonal-mean ice thickness deduced by *Hemingway & Mittal 2019* (*18*). Thick ice at the equator with a poleward thinning trend is notable. The ice shell over the south pole is only 6 km thick, a fifth of the equatorial ice shell. Such ice thickness variations have two effects. First, thick equatorial ice creates high pressure, depressing the local freezing point and leading to a roughly 0.1 K depression of the temperature just beneath the ice compared to the poles, assuming the interface is at the melting temperature (solid curve in Fig.1b). Second, thickness variations will drive ice to flow from thick-ice regions to thin-ice regions on million-year time-scales (*39–42*). To compensate the smoothing effect of the ice flow, ice must form in low latitudes and melt in high latitudes. Assuming an ice rheology, we can calculate ice flow speeds using an upside-down shallow ice model (details are given in section 4.4). In this way, we can infer the freezing/melting rate needed to maintain the observed ice geometry, as shown by the dashed curve in Fig.1b. Over time, this freezing and melting will lead to a meridional salinity gradient through brine rejection and fresh water input which, in steady state (assumed), must be balanced by salinity transport in the ocean.

The combined effect of these temperature and salinity forcings associated with the ice topography is to make equatorial waters saltier and colder than polar waters. This equator-to-pole temperature and salinity contrast, denoted as $\Delta\theta$ and ΔS, jointly affects the equator-to-pole density contrast $\Delta\rho$ through

$$\Delta\rho = \rho_0(-\alpha_T\Delta\theta + \beta_S\Delta S), \tag{1}$$

where ρ_0 is the reference density of water, and α_T and β_S are the thermal expansion and haline contraction coefficient, respectively. In a salty ocean, where water volume contracts when it is cold ($\alpha_T > 0$), we expect the ocean to sink at the cold low latitudes, because the water is dense there (see Fig. 2b). In contrast, in a fresh ocean ($\alpha_T < 0$) the opposite is possible because of seawater's anomalous expansion upon cooling (see Fig. 2a). In addition, the salinity anomalies induced by freezing/melting increasingly diminish as the assumed ocean salinity approaches zero. Thus the global overturning circulation in very salty and very fresh oceans can be expected to be of opposite sign. However, irrespective of which direction the ocean circulates, heat will be converged toward the equator, because of the mixing between cold equatorial water and warm polar water induced by the circulation. Limited by the efficiency of conductive heat loss through the thick equatorial ice, the equatorward heat convergence cannot be arbitrarily strong. This suggests that knowledge of ocean heat transport under various salinities and core-shell heat partitions can be used to discriminate between these different scenarios through examination of the heat budget of the ice,

In order to study the possible ocean circulations and heat transports on Enceladus in this way, we set up a zonally-averaged ocean circulation model to sweep across a range of mean salinities ($S_0 = 4$, 7, 10, 15, 20, 25, 30, 35 and 40 psu) and core-shell heat partitions (0-100%, 100-0% and 20-80%). Our model has its ocean covered by an ice shell that resembles that of the present-day Enceladus (*18*) (solid curve in Fig.1b), which is assumed to be sustained against the ice flow by a prescribed freezing/melting q (gray dashed curve in Fig.1b), regardless of the ice shell's heat budget. By prescribing q, we guarantee the ice shell to be in mass balance and we cut off the positive feedback loop between the ocean heat transport and the ice freezing/melting rates, thus preventing the simulated circulation from seeking a completely new state. When heat production by the silicate core is assumed to be non-zero, an upward heat flux at the bottom is prescribed. Guided by models of tidal heating described in section 4.4, this is assumed to be slightly polar-amplified (see purple curve in Fig.1d). By design, the globally integrated heat budget is guaranteed to be in balance.

At the water-ice interface, a downward salinity flux $S_0 q$ is imposed to represent the brine rejection and freshwater production associated with freezing/melting. Meanwhile, the ocean temperature there is restored toward the local freezing point. Thus the ocean will deposit heat to the ice when its temperature is slightly higher than the freezing point, and vice versa. In order for the heat budget of the ice to close, this ocean-ice heat exchange $\mathcal{H}_{\mathrm{ocn}}$, together with the tidal heat produced in the ice $\mathcal{H}_{\mathrm{ice}}$ (red curve in Fig. 1d) and the latent heat released $\mathcal{H}_{\mathrm{latent}}$ ($\mathcal{H}_{\mathrm{latent}} = \rho L_f q$, where ρ and L_f are the density and fusion energy of ice, see the gray curve in Fig. 1d) should balance the conductive heat loss through the ice shell $\mathcal{H}_{\mathrm{cond}}$ (green curve in Fig. 1d). Since the freezing/melting rate is not allowed to respond to the simulated ocean-ice heat exchange, the aforementioned heat budget is not necessarily in balance, and the extent to which it is not informs us of the plausibility of the assumed salinity and heat partition.

Before going on to describe our results, we emphasize that we have adopted a zonally-averaged modeling framework so that we can readily explore parameter space whilst integrating out to an equilibrium state, which takes about 10,000 model years. This necessarily implies that our ocean model is highly parameterized — as are the models of tidal heating and ice flows that are used to provide the forcing at the boundaries that drive it — and so have many unavoidable uncertainties. In particular, as described in detail in section 4.2 and just as in terrestrial ocean models, processes such as convection, diapycnal mixing and baroclinic instability are parameterized guided by our knowledge of the mechanisms that underlie them.

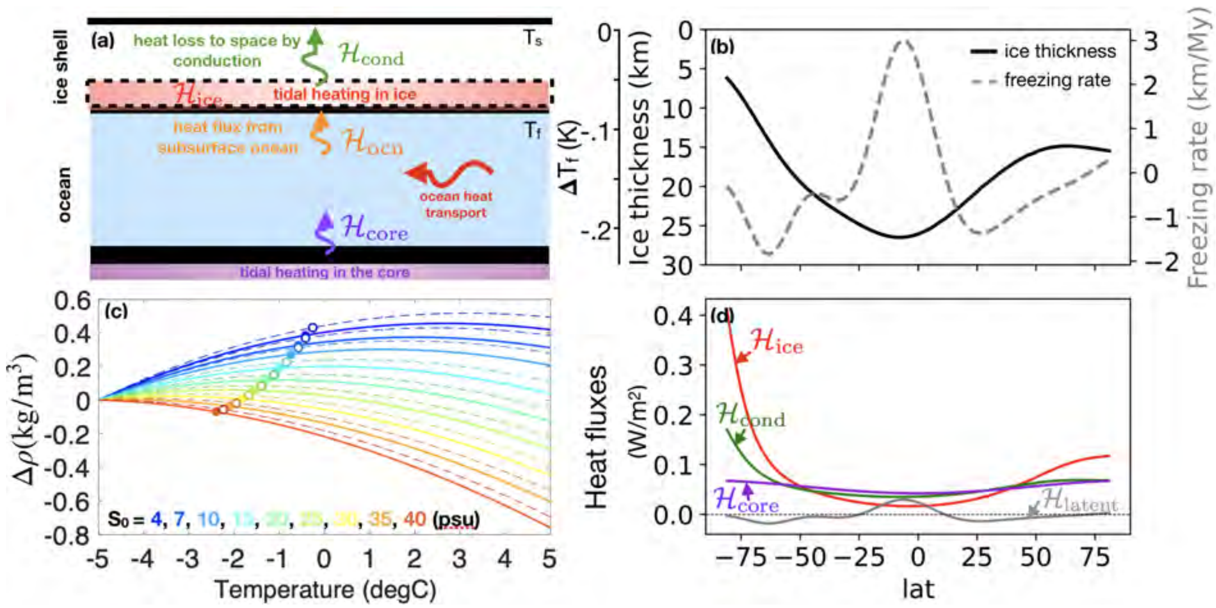

Figure 1: Panel (a) presents the primary sources of heat and heat fluxes in an icy moon which include: heating due to tidal dissipation in the ice $\mathcal{H}_{\rm ice}$ and the silicate core $\mathcal{H}_{\rm core}$, the heat flux from the ocean to the ice $\mathcal{H}_{\rm ocn}$ and the conductive heat loss to space $\mathcal{H}_{\rm cond}$. Ocean heat transport is shown by the horizontal arrow. Panel (b) shows the observed ice shell thickness of Enceladus based on shape and gravity measurements (*18*) (black solid curve, left y-axis). The suppression of the freezing point of water by these thickness variations, relative to that at zero-pressure, is indicated by the outer left y-axis. The gray dashed curve shows the freezing (positive) and melting rate (negative) required to maintain a steady state based on an upside-down shallow ice flow model (y-axis on the right). Panel (c) shows how the density anomaly of water varies as its temperature varies around -5°C as a function of salinity. Moving from cold to warm colors denotes increasing salinity, as indicated by the colored lettering. The solid (dashed) curves are computed assuming the pressure under the 26.5 km (5.6 km) of ice at the equator (south pole). The freezing points are marked by the circles. Panel (d) shown typical magnitudes and profiles of $\mathcal{H}_{\rm ice}$, $\mathcal{H}_{\rm core}$, $\mathcal{H}_{\rm cond}$ and $\mathcal{H}_{\rm latent}$. The models of heat fluxes and ice flow on which all these curves are based can be found in section 4.4.

2 Results

2.1 Patterns of ocean circulation, temperature and salinity

Due to the relatively low freezing point (Fig. 1c) and elevated freezing rate (Fig. 1b) of low latitudes, water just under the ice is colder and saltier than near the poles, regardless of the mean

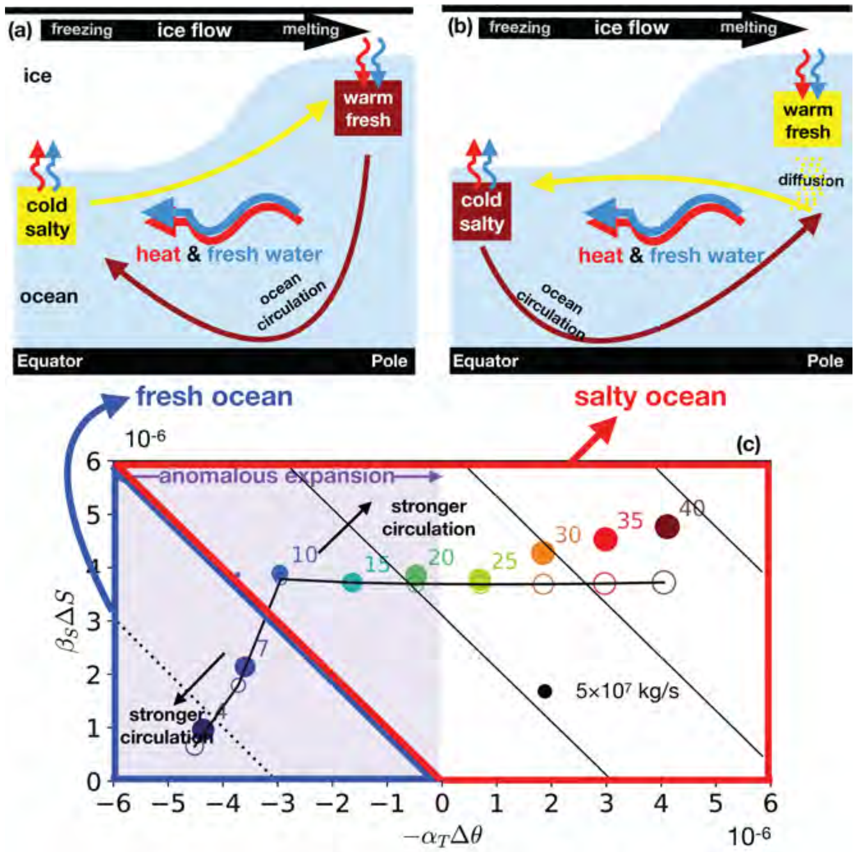

Figure 2: At the top we show schematics of ocean circulation and associated transports of heat (red wiggly arrows) and fresh water (blue wiggly arrows) for (a) a fresh ocean in which $\alpha_T < 0$ and (b) a salty in which $\alpha_T > 0$. Dark brown arrows denote sinking of dense water, light yellow arrows denote rising of buoyant water. The circulations are forced by the freezing/melting required to counterbalance the down-gradient ice flow (thick black arrows marked at the top) and by variations in the freezing point of water due to pressure, as presented in Fig.1b. In panel (c), we present a regime diagram, showing the influence of temperature and salinity anomalies on density assuming different salinities (the number on the shoulder of each circle gives the S_0 used in that experiment), and how the overturning circulation of the ocean responds in GCM simulations and our conceptual model. Horizontal and vertical axes are the equator-to-pole density contrast associated with temperature and salinity anomalies, $-\alpha_T \Delta\theta$ and $\beta_S \Delta S$. Both ΔS and $-\Delta\theta$ are positive (the equator is always saltier and colder than the pole), and they are computed by taking the difference between the maximum and the minimum within the northern hemisphere. The sign of the coordinates reflect the sign of α_T and β_S: β_S is always positive, but α_T increases from negative to positive as S_0 increases. In the high/low S_0 experiments, the signs of $-\alpha_T \Delta\theta$ and $\beta_S \Delta S$ are the same/opposite. Red (blue) solid lines delineate the salty (fresh) ocean regimes. Purple shading highlights the regime where anomalous expansion of seawater is present with negative α_T so that warming leads to sinking. The size of each circle represents the amplitude of the overturning circulation (the peak Ψ occurs in the northern hemisphere). The 45° tilted black lines are isolines of the equator-to-pole density difference $\Delta\rho$. Solid lines denote dense water near the equator and dotted lines denote dense water over the poles. As illustrated by the black arrows, circulation strengthens with $\Delta\rho$ moving away from the transition line between the fresh and salty ocean. The empty circles connected by a black solid curve show the fit of the conceptual model developed in Section 2.3 which broadly captures the behavior of the explicit calculation using our full model.

salinity. This pole-to-equator temperature and salinity contrast leads to variations in density, which in turn drive ocean circulation. In Fig. 3(c,e), we present the density anomaly, $\rho_0(\alpha_T\theta' + \beta_S S')$, and the meridional overturning streamfunction $\Psi(\phi, z) = \int_{-D}^{z} \rho(\phi, z')V(\phi, z')\times(2\pi(a-z')\cos\phi)\, dz'$. Here, θ' and S' (plotted in Fig. 3a,b) are the deviation in potential temperature and salinity from the reference, V is the meridional current, ρ_0 is the water density, and D is the ocean depth, ϕ denotes latitude and z points upwards.

Since, depending on the mean salinity, the density gradient induced by temperature variations can either enhance or diminish that induced by salinity, the overturning circulation can sink either over the poles or over the equator. When S_0 is greater than 22 psu, water expands with increasing temperature ($\alpha_T > 0$, see reddish curves in Fig.1c, 2 MPa pressure assumed). As a result, the cold and salty water under the thick equatorial ice shell is denser than polar waters, as shown in Fig.3-c3 and sketched in Fig. 2b using the dark brown color. Equatorial waters therefore sink, as shown in Fig.3-e3 (indicated in Fig.2b using the dark brown arrow), constrained by the direction of the rotation vector (marked by the black dashed curves).

However, when S_0 is below 22 psu, the thermal expansion coefficient changes sign ($\alpha_T < 0$, as shown by the bluish curves in Fig.1c). This so-called anomalous expansion of water results in the temperature-induced density difference and the salinity-induced density difference partially cancelling one another, giving rise to two possibilities. If the salinity factor dominates, the overturning circulation becomes one of sinking at the equator, as show in Fig.3-d2 and sketched in Fig.2b using a dark brown arrow. But if the temperature factor dominates, the overturning circulation flips direction with sinking over the poles (Fig.3-d1 and Fig.2a) because water is denser there (Fig.3-c1). The switch in overturning circulation with salinity can also occur in models of Earth's ocean (*26, 27*), even though Earth's ocean is forced mostly by wind stress.

The transition from polar to equatorial sinking is governed by the density difference between the poles and the equator. Taking the north pole as a reference, the temperature-related density

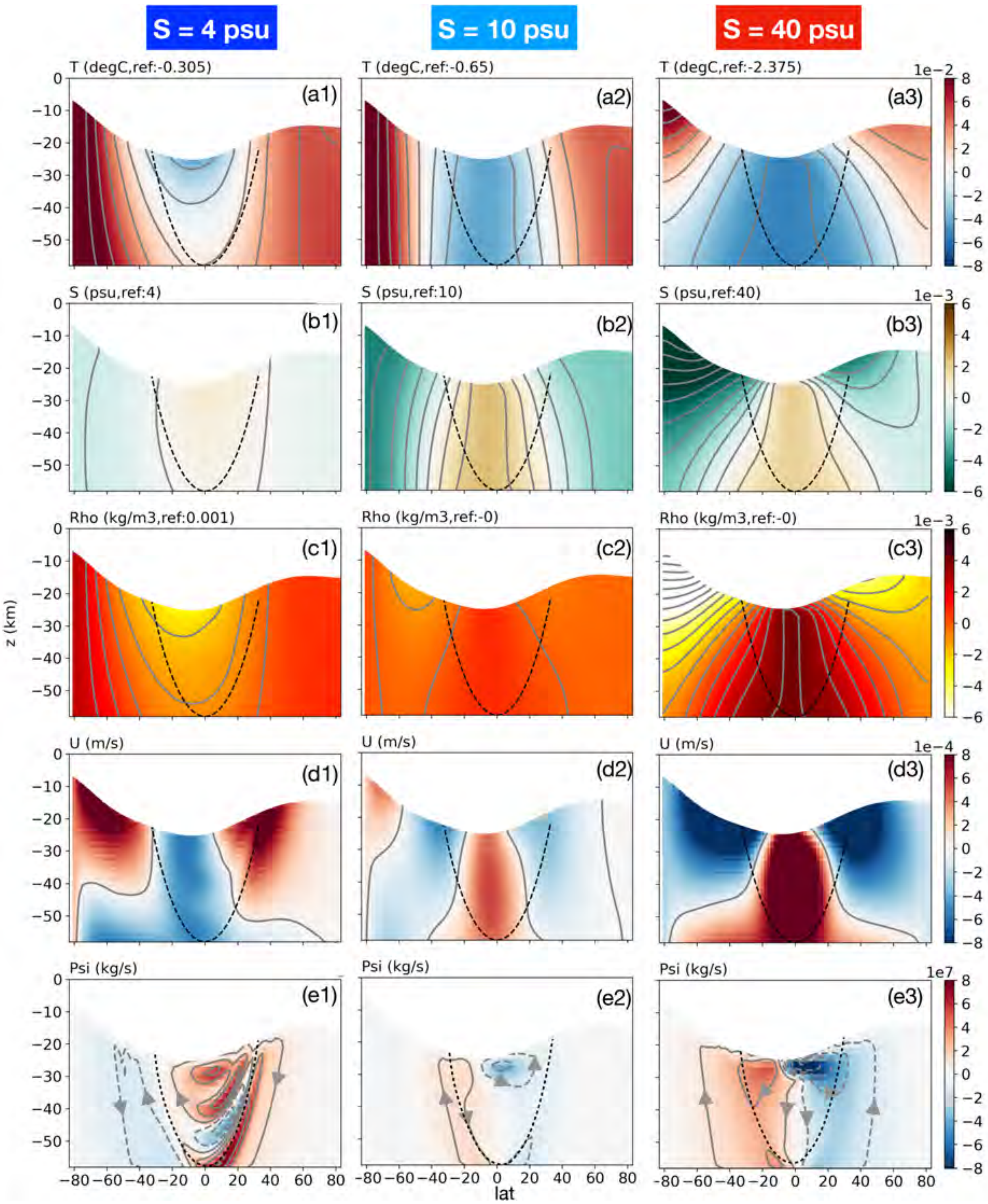

Figure 3: Ocean circulation and thermodynamic state for experiments driven by freezing/melting of ice and under-ice temperature distributions shown in Fig. 1b for oceans with various mean salinities. Moving from top to bottom we present temperature T, salinity S, density anomaly $\Delta\rho$, zonal flow speed U and meridional overturning streamfunction Ψ with arrows indicating the sense of flow. The left column presents results for a low salinity ocean ($S_0 = 4$ psu), the right column for high salinity ($S_0 = 40$ psu), and the middle column for an ocean with intermediate salinity ($S_0 = 10$ psu). The reference temperature and salinity (marked at the top of each plot) are subtracted from T and S to better reveal spatial patterns. Positive U indicates flow to the east and positive Ψ indicates a clockwise overturning circulation. Black dashed lines mark the position of the tangent cylinder, an imaginary cylinder which is parallel to the rotation vector and touches the core.

anomaly at the equator can be written as $-\alpha_T \Delta\theta$, and the salinity-related density anomaly as $\beta_S \Delta S$, where $\Delta\theta$ and ΔS are the potential temperature and salinity anomaly at the equator relative to the north pole. Fig.2c presents the strength of the overturning circulation from all nine experiments in the $(-\alpha_T \Delta\theta,\ \beta_S \Delta S)$ space: the size of the circles are proportional to Ψ. The 45 degree tilted line denotes perfect cancellation between the saline and temperature-driven overturning circulations: it passes near 10 psu, explaining why the 10 psu experiment has the weakest circulation compared to all others. On moving away from this line in either direction the strength of the overturning circulation increases but is of opposite sign, as represented schematically in Fig. 2a,b.

The overturning circulation shapes the tracer distributions and the zonal currents. Downwelling regions (low latitudes for a salty ocean and high latitudes for a fresh ocean) advect density, temperature and salinity anomalies, set at the ocean-ice interface, into the interior ocean. Note the bending of the temperature and salinity contours equatorward (poleward) when downwelling occurs at the poles (equator), as shown in Fig. 3. This results in meridional density gradients which are in a generalized thermal wind balance with zonal currents in which all components of the Coriolis force are included. (Fig. 3d).

Thus far, we have assumed zero heat flux from the bottom. With all the required heating generated in the silicate core (core-heating), a salty ocean will become more convectively unstable, whereas a fresh ocean will become more stably stratified due to the negative thermal expansion coefficient (see Fig.S1-c in the SM). As a result, the overturning circulation strengthens (weakens) in a salty (fresh) ocean. The temperature/salinity profiles and even the circulation patterns remain qualitatively similar to the shell-heating scenarios, especially for the salty scenarios, because the heating-induced bottom-to-top temperature difference is typically only a few tens of milliKelvin when convection is active, much smaller than the equator-to-pole temperature difference induced by the freezing point variations (Fig.3) which is order 0.1 Kelvin —

see Fig.1b,c. The vertical temperature gradient induced by the bottom heating is much larger in a fresh ocean because of the suppression of convection by anomalous expansion. The strengthening of vertical temperature gradient largely enhances the OHT, even though the circulation is weakened slightly.

It is important to note that the ocean circulation we have obtained here penetrates throughout the entire depth of the ocean, much deeper than suggested by *Lobo et al. 2021* (*43*) based on a more idealized ocean model. This is despite the fact that the forcing amplitude assumed in (*43*) is a full 3 orders of magnitude larger. Our circulation is deep because, in the absence of strong viscosity, the circulation in the ocean interior aligns with the direction of the rotation axis (see Fig. 3-e), a consequence of the Taylor-Proudman theorem. Only adjacent to the ice shell and the seafloor, can currents flow across the direction of the tangent cylinder (see Bire et al for a discussion of the importance of the tangent cylinder). Moreover, in all the shell-heating scenarios, the downwelling regions are convectively unstable, allowing dense water formed near the surface to sink all the way to the bottom.

This is rather different from the physical picture presented by *Lobo et al. 2021* (*43*), who describe an ocean which is strongly stratified and whose circulation is confined near the ice shell. Such differences likely stem from the values adopted for the eddy diffusivity representing baroclinic instability, $\kappa_{\rm GM}$, and diapycnal diffusivity associated with convective mixing, $\kappa_{\rm conv}$: *Lobo et al. 2021* (*43*), assume a very large value of $\kappa_{\rm GM} = 1000\ m2/s$ based on observations of earth's ocean, and a rather small $\kappa_{\rm conv} = 0.01\ m2/s$ for the convective regions over the poles. This dominance of lateral baroclinic instability over vertical convection gives rise to very strong stratification which in turn confines the vertical extent of the circulation. Instead, here we estimate an eddy diffusivity appropriate to Enceladus to be of order 0.3 m^2/s based on energetic arguments (*44*) (see section 4.2 for a derivation) and a convective mixing rate to be order 1 m^2/s based on the scaling laws governing convection in a rapidly rotating system (*45*).

In this parameter setting, the stratification is weak and almost half of the ocean is convecting due to loss of buoyancy through interaction with the ice.

2.2 Ocean heat transport and the heat budget of the ice shell

We have seen that the freezing point depression of water due to pressure results in the polar oceans being warmer than the tropical ocean just beneath the ice, because the ice is thin at the poles relative to the equator. One might expect, then, that OHT would be directed equatorward — from warm to cold — irrespective of the sense of the ocean's overturning circulation. The amplitude of OHT, which is proportional to the overturning strength multiplied by a temperature contrast, (*46*), will depend on the strength of the circulation, which in turn depends on ocean salinity and the heat partition between the core and the ice shell. As can be clearly seen in Fig. 4(a,d), heat is indeed converged toward the equator in all scenarios. However, due to the cancellation between temperature- and salinity-driven circulation, the heat convergence in an ocean with an intermediate salinity is a small fraction of that in the end-member cases. If there is no tidal heating produced in the ice shell, such an equatorward OHT will inevitably melt the ice shell over the equator because the conductive heat loss is smaller there due to the relatively thick ice shell. In addition, ice will be transported poleward, from thick to thin, accelerating the flattening of the ice shell. Therefore, in order to sustain the observed ice geometry (*18*), a polar-amplified tidal heating in the ice is necessary which has a meridional gradient strong enough to compensate equatorward OHT.

To quantify the impact of OHT on ice geometry, we compute the heat flux transmitted from the ocean to the ice $\mathcal{H}_{\rm ocn}$ and diagnose how much tidal heating is required in the ice shell to close the ice's heat budget,

$$\hat{\mathcal{H}}_{\rm ice} = \mathcal{H}_{\rm cond} - \mathcal{H}_{\rm ocn} - \rho_i L_f q. \tag{2}$$

The $\hat{\mathcal{H}}_{\rm ice}$ inferred from our various ocean circulations is shown by the solid curves in Fig.4(b,e) for the shell-heating and core-heating scenarios, respectively. If all is consistent, this inferred ice dissipation rate should be close to the estimate given by a tidal dissipation model $\mathcal{H}_{\rm ice}$ (details of the model can be found in section 4.5), which is shown in the same figure using black dashed curves. The tidal dissipation model. of course, is also subject to significant uncertainties due to our limited understanding of the ice rheology, but it should be positive definite. However, for many assumed salinities (very fresh and very salty), the implied tidal heating is actually large and negative!, indicating that these scenarios are incompatible with the observed ice geometry and therefore less likely.

We measure the mismatch between $\hat{\mathcal{H}}_{\rm ice}$ and $\mathcal{H}_{\rm ice}$ by the following index,

$$I_{\rm mis} = \sqrt{\overline{\left(\frac{\hat{\mathcal{H}}_{\rm ice} - \mathcal{H}_{\rm ice}}{\max\{\mathcal{H}_{\rm ice}, 20\ \mathrm{mW/m^2}\}}\right)^2}}, \tag{3}$$

where the over-bar represents a global area-weighted average, and the max function in the denominator helps avoid the singularity when $\mathcal{H}_{\rm ice} \to 0$. We show the shell-heating and core-heaing mismatch indices $I_{\rm mis}$ as a function of the ocean salinity in Fig.4(c,f) using filled dots.

The dependence of $I_{\rm mis}$ on ocean salinity in the shell-heating scenarios. Although OHT is always equatorward, those ocean solutions with a strong overturning circulation (e.g., $S_0 = 4,\ 40$ psu) focus large amounts of heat into low latitudes, resulting in a heat budget discrepancy of almost 80 mW/m^2 (see Fig. 4b), twice the global-mean heat production rate; if used to melt ice, a rate of 7.5 km/Myr would result. Near the equator, $\hat{\mathcal{H}}_{\rm ice}$ even becomes significantly negative, conflicting with the need for tidal dissipation to be positive definate. This is reflected in the relatively large values of $I_{\rm mis}$ evident in Fig. 4(c). The heat budget improves significantly at intermediate salinities, and the best match is achieved in the $S_0 = 10$ psu scenario. This corresponds to the near-cancellation of the temperature and salinity-induced density anomalies (see Fig.2c).

It is interesting to note that the increase in the mismatch is steeper on the fresh side of 10 psu than the salty side (Fig.4c). This is related to the different energetics of ocean circulation in a very fresh ocean close to the freezing point (where $\alpha_T < 0$) and a salty ocean (where $\alpha_T > 0$). As pointed out by *Zeng & Jansen 2021* (*25*), if the buoyancy gain at the equator is deeper in the water column than the buoyancy loss at the poles then ocean circulation can always be energized since dense polar water higher up the water column is transported to depth. However, in a salty ocean the opposite is true and equatorial dense water cannot be drawn upward to the polar ice shell without invoking diffusive processes (*47*). This difference can be seen in Fig.3-e. The overturning circulation in the fresh ocean (Fig.3-e1) can directly connect the water-ice interface at the pole to equatorial regions; in contrast in a salty ocean (Fig.3-e3), the circulation weakens moving poleward and almost completely vanishes in the fresh water lens formed under the polar ice shell. Strong stratification develops in the diffusive layer (Fig.3-c3) which sustains an upward buoyancy flux without strong circulation, as indicated in the schematic diagram Fig.2b.

Dependence on the core-shell heat partition. Since, in realistic scenarios, the bottom-to-top temperature difference induced by core heating is far smaller than the equator-to-pole temperature difference induced by the freezing point variations, the circulation patterns and temperature/salinity profiles of the core-heating solutions remain broadly the same as those in which shell-heating dominates (see Fig. 3 and Fig.S1). As a result, the OHT and $\hat{\mathcal{H}_{\rm ice}}$ are qualitatively similar too, as can be seen in Fig. 4(d,e). What is different, however, is that the core-heating cases have, by construction, zero heat production in the ice shell and so equatorward OHT and polar-amplified conductive heat loss can no longer be effectively compensated by polar-amplified dissipation in the ice shell. Over the thin polar ice, heat lost to the space is much more efficient than elsewhere and, furthermore, OHT is equatorward. Thus polar ice will accumulate over time in the absence of local heating within it (black dashed curved in panel e). Indeed the

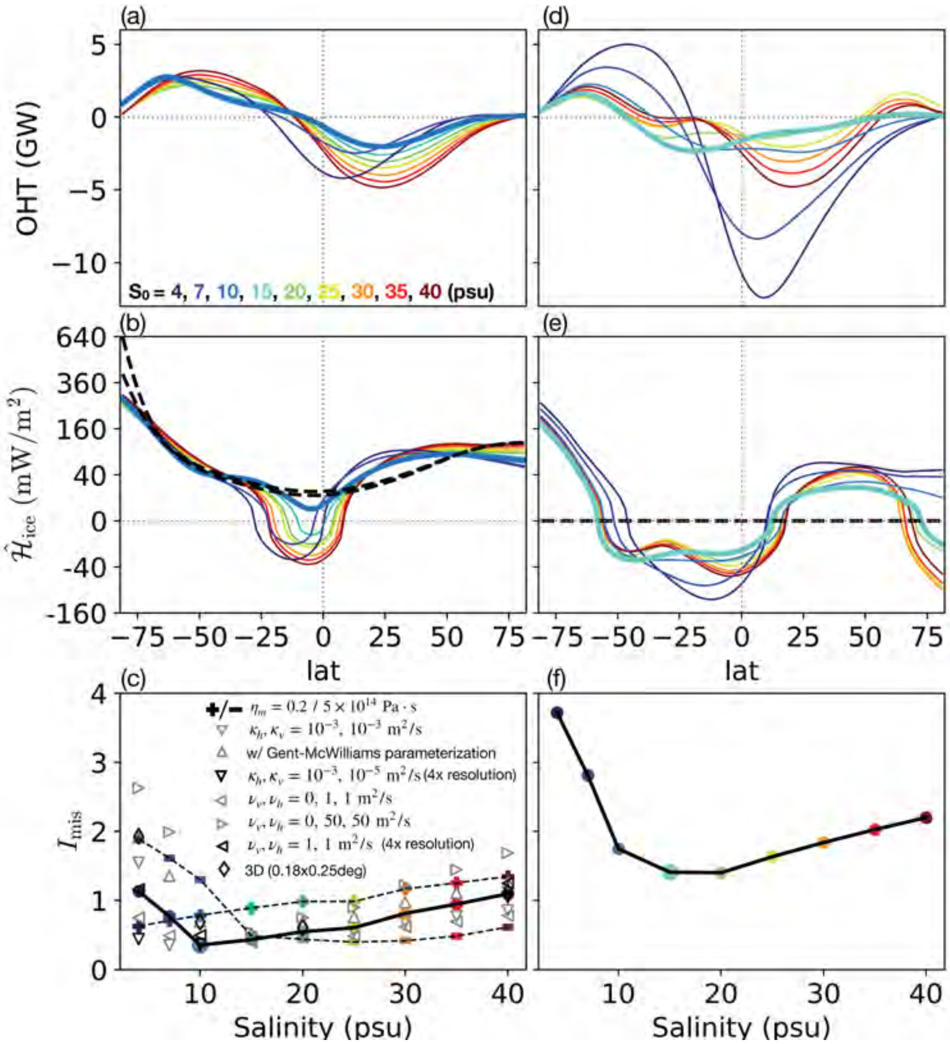

Figure 4: Meridional heat transport and heat budget for the shell-heating scenario (left) and the core-heating scenario (right). The top panels show the vertically-integrated meridional OHT for various assumed S_0. Positive values denote northward heat transport. The middle panels show the inferred tidal heating $\hat{\mathcal{H}}_{\mathrm{ice}}$. Note that the y-axis is not linear. The two black dashed curves in panel (b) are the profiles of $\mathcal{H}_{\mathrm{ice}}$ predicted by a model of tidal heating in the ice shell with $p_\alpha = -2$ and $p_\alpha = -1$, respectively: a more negative p_α indicates a stronger rheology feedback and thus yields a slightly more polar-amplified $\mathcal{H}_{\mathrm{ice}}$ profile. The black dashed curves in panel (e) coincide with the zero line, because $\mathcal{H}_{\mathrm{ice}} = 0$ when all the heating is in the core. The heat transport and inferred tidal heating profiles corresponding to the best-match experiments are highlighted by thicker curves in the top and middle rows. The bottom panels show the mismatch index I_{mix}, defined in Eq. (3). Filled colored dots connected by a thick solid line correspond to the default setup (GM diffusivity $\kappa_{\mathrm{GM}} = 0.1$ m^2/s, horizontal/vertical diffusivity $\kappa_h = \kappa_v = 0.005$ m^2/s, horizontal/vertical viscosity $\nu_h = \nu_v = 10$ m^2/s, 100% heat produced in the ice shell, and melting-point ice viscosity $\eta_m = 10^{14}$ Pa·s). Plus and minus symbols represent sensitivity tests to ice viscosity and gray symbols represent sensitivity tests to mixing coefficients and model resolution. The I_{mix} of the low and high η_m experiments are multiplied by a factor of 0.3 and 2, respectively, so that all plots make use of the same scale.

mismatch indices for the core-heating scenarios are higher overall as shown by Fig. 4f. More detailed discussions of the bottom heating solutions can be found in section 1.1 of the SM.

Sensitivity tests. To explore sensitivity to parameter choices, we carried out many sets of experiments changing the assumed ice rheology, mixing rates in the ocean and model resolution. By default, the melting point ice viscosity η_m is set to 10^{14} Pa·s, an intermediate value between an estimated lower bound of 10^{13} Pa·s and an upper bound of 10^{15} Pa·s (*39*). In the ice rheology sensitivity test, we examined $\eta_m = 2 \times 10^{13}$ Pa·s and $\eta_m = 5 \times 10^{14}$ Pa·s. A lower (higher) ice viscosity induces stronger (weaker) ice flows, which require a greater (smaller) balancing freezing/melting rate; this in turn enhances (suppresses) the salinity flux imposed upon the ocean, giving rise to larger (weaker) salinity gradients. Compensating the density anomaly implied by this salinity gradient thus requires a more (less) negative α_T and lower S_0. As shown by the plus signs in Fig. 4c, the best matching S_0 is indeed reduced from 10 psu to 4 psu (the full solution is summarized in Fig.S2 of the SM) with $\eta_m = 2 \times 10^{13}$ Pa·s and increased from 10 psu to 15-30 psu (the full solution is summarized in Fig.S3 of the SM) with $\eta_m = 5 \times 10^{14}$ Pa·s. Because of the stronger latent heating, the overall matching significantly deteriorates in experiments with lower ice viscosity. Note that in the $\eta_m = 2 \times 10^{13}$ Pa· sensitivity test a factor of 0.3 premultiplies I_{mis} so that the same scale can be used in all plots.

The dissipation rate within the ocean driven by libration/tidal motions is also under debate (*21, 23, 48*) leading to a wide range of possible diapycnal diffusivities. Assuming a dissipation rate given by *Rekier et al. 2019* (*21*), we estimate a vertical diffusivity for Enceladus to be around 5×10^{-3} m^2/s (see section 4.2), which is orders of magnitude greater than the molecular diffusivity. To place this in context, *Zeng & Jansen 2021* (*25*) suggest that the vertical diffusivity can reach 3×10^{-3} m^2/s. This is the diffusivity assumed in our default experiment for both the vertical and horizontal directions. To explore solution sensitivity we carried out experiments with different horizontal/vertical explicit diffusivity $\kappa_h,\ \kappa_v$, and horizontal/vertical viscosity ν_h, ν_v. We also explored sensitivity to the parameterization of baroclinic instability by varying the eddy diffusivity used in the Gent and McWilliams scheme (*49*). The resulting $I_{\rm mis}$ in these sensitivity experiments are plotted on Fig. 4c using triangular markers. Just as in the control (solid line with filled dots), $I_{\rm mis}$ first decreases then increases as the ocean salinity is changed, and a minimum is achieved near 10 psu. Among all the sensitivity tests, those with lower diffusivities/viscosities result in a weaker OHT (see panel-e of Fig.S4,5,8,9) and better matching of the heat budget. However, in the least diffusive experiments ($\kappa_h = 10^{-3},\ \kappa_v = 10^{-5}$ m^2/s), the heat budget matching over the polar regions deteriorates due to the strong temperature gradient developed under the ice shell, as indicated by the downward black triangles in Fig.4c. More detailed discussions of these sensitivity tests can be found in SM section 1.3.

Sensitivity to model resolution and 3D representation of dynamics has also been explored. In Fig. 4c, the black leftward triangles show results for the low viscosity sensitivity test repeated using $4\times$ resolution. The general trend of $I_{\rm mis}$ against salinity remain unchanged but the matching deteriorates for the fresh ocean scenario due to strong heat transport (See Fig.S10 in the SM). Also shown are results from 3D simulations (black diamonds). These experiments are continued on from an equilibrated 2D solution, and have a horizontal resolution of $0.18{\times}0.25°$, and a vertical resolution of 500 m. A Smagorinsky viscosity parameterization ($\nu_{\rm smag} = 4$) is used in place of high explicit viscosity to allow improved treatment of the dynamics. The $I_{\rm mis}$ again achieves a minimum at intermediate salinities. Vertical and horizontal sections through the solution are presented in Fig.S10 and Fig.S11 in the SM. We note that even at this resolution, we are barely able to resolve eddy dynamics. More detailed analysis and exploration of 3D dynamics requires much higher resolution than we can afford here.

Finally, we note that there is heat transported across the equator into the southern hemisphere in all our experiments. Depending on the model setup, the amplitude ranges from a few GW to tens of GW, which is a significant fraction of the 35GW of heating being generated by the tide. If this southward heat transport pattern were to also exists when the ocean is fully coupled to the ice, it will provide a mechanism to induce hemispheric symmetry breaking of the ice thickness, in addition to the ice-rheology feedback proposed by *Kang & Flierl 2020* (*50*).

2.3 Exploring mechanisms with a conceptual model

The numerical solutions presented above suggest that if Enceladus' ocean is of intermediate salinity with cancelling salinity and temperature-driven overturning circulations, then equatorial convergence of heat is minimized, allowing a thick equatorial ice shell to be maintained. This is much less likely in very fresh or very salty oceans. Here, we use a conceptual model that is similar to that of Stommel (*51*) to highlight the physical processes that control the circulation strength and explore a wider range of parameter space that can be applied to other icy moons.

We represent the overall density contrast using the equator minus north pole density difference $\Delta\rho$. The temperature-related density anomaly is $-\alpha_T\Delta\theta$, and salinity-related one is $\beta_S\Delta S$, where $\Delta\theta$ and ΔS are the potential temperature and salinity anomaly at the equator relative to the north pole. We expect the circulation-induced mass exchange between the equatorial and polar regions, denoted by ψ, to vary proportionally with $\Delta\rho$ (Eq. 1). For simplicity, we assume a linear form

$$\psi = A(-\alpha_T\Delta\theta + \beta_S\Delta S), \tag{4}$$

where the constant A (units: kg/s) maps the density contrast on to the vigor of the overturning circulation, $\beta_S \approx 8 \times 10^{-4}$/psu for all S_0, but α_T depends sensitively on S_0, as given by the Gibbs Seawater Toolbox (*24*). A positive ψ corresponds to a circulation that sinks at the equator, and vice versa.

The temperature contrast $\Delta\theta$ is determined by the pressure-induced freezing point shift from the north pole to the equator,

$$\Delta\theta = b_0 \Delta P = b_0 \rho_i g \Delta H, \tag{5}$$

where $b_0 = -7.61 \times 10^{-4}$ K/dbar, $\rho_i = 917$ kg/m^3 is the ice density, $g = 0.113$ m/s^2 is the surface gravity of Enceladus and $\Delta H = 11$ km is the difference in ice thickness between the equator and the north pole.

The lateral salinity flux is given by the product of ψ and a salinity contrast ΔS and balances the salinity flux due to freezing and melting yielding (see a detailed derivation in *Marshall & Radko 2003* (*52*)):

$$(|\psi| + \psi_{\text{base}})\Delta S = \rho_0 S_0 \Delta q \times (\pi(a - H_0)^2) \tag{6}$$

Here, Δq, the difference in the freezing rate between low and high latitudes, is chosen to be 2 km/Myr based on Fig.1b, and ψ_{base} is the circulation due to the imperfect cancellation between temperature- and salinity-induced buoyancy forcing. $a = 250$ km is the radius of Enceladus, $H_0 = 20.8$ km is the mean thickness of the ice shell and S_0 is the mean salinity. The fact that ψ and ΔS appear as a product indicates that the salinity gradient will weaken as the overturning circulation strengthens for fixed salinity forcing.

Combining Eq (4), Eq (5) and Eq (6), we can solve for ΔS and ψ. The only tunable parameter here is A, which controls the strength of the overturning circulation and can be adjusted to fit that obtained in our ocean model. With $A = 10^{13}$ kg/s and $\psi_{\text{base}} = 2 \times 10^7$ kg/s (based on Fig. 3-e2), we obtain the solutions shown by the open circles in Fig.2c (the size of the circle reflect the amplitude of $|\psi| + \psi_{\text{base}}$). The conceptual model solution broadly captures the behavior of the numerical simulations (filled circles), including the strengthening of the overturning circulation and the weakening of salinity gradient away from the transition zone separating the alpha ocean and beta ocean.

When $S_0 < 22$ psu, $\alpha_T \Delta\theta$ and $\beta_S \Delta S$ take opposite signs, and depending on which one has a greater absolute value, the circulation ψ can be in either direction. Each possibility corresponds to one solution. The solution in the fresh ocean regime matches the numerical model results. The solution in the salty ocean regime (marked by a cross mark in Fig.2) requires an extraordinarily strong salinity gradient to dominate the negative $\alpha_T \Delta\theta$. This is only possible when the mixing is extremely weak, i.e., when the temperature- and salinity-induced circulation almost exactly cancel one-another out, and no other forms of mixing exists, somewhat implausible.

What is the all-important heat flux implied by our conceptual model? Analogously to Eq (6), the meridional heat transport can be written

$$\mathcal{H}_{\rm ocn} = \frac{C_p |\psi| \Delta\theta}{\pi(a - H_0)^2}. \tag{7}$$

This is shown as a function of salinity and equator-to-pole thickness variations in Fig.5a. Recall that the water-ice heat exchange must be smaller than the heat conduction rate of 50 mW/m^2 to maintain observed thickness variations of the Enceladus ice shell. The likely parameter regime is shaded yellow (*14–18*). We see that a salinity between roughly 7-22 psu (marked by two vertical blue dashed lines) is required to maintain ice thickness variations as large as are seen on Enceladus.

3 Discussion

In conclusion, from knowledge of the geometry of the ice shell on Enceladus we have deduced likely patterns of (i) salinity gradients associated with freezing and melting and (ii) under-ice temperature gradients due to the depression of the freezing point of water due to pressure. We have considered the resulting ocean circulation driven by these boundary conditions, along with the effect of putative heat fluxes emanating from the bottom if tidal dissipation in the core is significant. We find that the ocean circulation strongly depends on its assumed salinity. If the ocean is fresh, sinking occurs at the poles driven by the meridional temperature gradient (Fig.3 first column); if the ocean is salty, sinking occurs at the equator driven by the salinity gradient

(Fig.3 third column). In both cases, heat is converged toward the equator as the warm polar water is mixed with the cold equatorial water.

In the absence of polar-amplified ice dissipation to counterbalance equatorward heat transport, the polar (equatorial) ice shell will inevitably freeze (melt), because the conductive heat loss through the ice shell also tends to cool polar regions. This, together with the tendency of ice to flow from regions where it is thick to thin, will flatten ice geometry in the core-heating scenarios. Ocean salinity and the heat partition between the core and the ice shell affect ocean circulation and thereby the heat budget, which should be close to balance — this provides us an opportunity to infer these properties using the relatively well-constrained ice shell geometry. It is found that scenarios without plenty of heat production in the shell cannot prevent the equatorial ice shell from being thinned by the equatorward heat convergence and the ice flow. Even when all heat is assumed to be produced in the ice shell, equatorward heat convergence in a very salty or very fresh ocean is implausibly strong to maintain a balanced heat budget. Instead, if heat production is assumed to occur primarily in the ice shell and salinity assumed to have an intermediate value (our calculations suggest between 7-30 psu), then temperature and salinity-driven overturning circulations largely cancel one-another and equatorward heat transport diminishes. If these conditions are met, polar-amplified dissipation in the ice shell can sustain a broadly balanced heat budget. As discussed in the introduction, such salinity ranges are consistent with those inferred from chemical equilibrium models of the interaction between the rocky core and the ocean (*34–36*).

Our study has focused on Enceladus, but it may also have implications for other icy moons. For example, Europa perhaps has a salinity in excess of 50 psu, as suggested by the strong magnetic induction field measured by the Galileo mission (*53*) — see *Zolotov & Shock 2001* (*54*), *Khurana et al. 2009* (*55*), *Vance et al. 2020* (*56*) for discussions of possible ocean compositions together with uncertainties. With a higher ocean salinity, ten times stronger gravity and a slower rotation rate, we expect the circulation coefficient A for Europa to be considerably higher than the value we have found here for Enceladus. That said, even if we adopt the lower Enceladus value of A, the implied OHT convergence beneath the ice shell of Europa near the equator still exceeds the conductive heat loss rate there, if the ice thickness variation exceeds 20% of the mean thickness (assuming ocean salinity is greater than 50 psu, see Fig. 5b). Thus our simple model leads us to believe that Europa may have a rather flat ice sheet. This is in line with the observation that the mean ice thickness on Europa is less than 15 km (best match is rather smaller at 4 km, see also (*57*) for other estimates) (*53, 58*). Moreover, no fissures that mimic the "tiger stripes" of Enceladus have been found on Europa. For icy moons with thicker ice shells, such as Dione, Titan, Ganymede and Callisto, the high pressure under the ice shell would remove any anomalous expansion unless the ocean is very fresh. This would make it impossible for temperature and salinity driven overturning circulations to cancel one another. Furthermore, ice flow becomes more efficient because, if all else is the same, it is proportional to the ice thickness cubed (see Eq. 24). Our conceptual model indeed indicates that icy ocean worlds with thick ice shells are likely to have small spatial shell thickness variations. This is consistent with shell thickness reconstructions based on gravity and shape measurements (*59–62*). With improved measurements of gravity, topography, and induced magnetic fields for icy moons made possible by future space missions (e.g., Europa Clipper), our conceptual model could provide a useful framework from to interpret them.

Finally, it should be noted that, given the simplifications made in our study, our quantitative results are far from conclusive. Instead of trying to put a solid constraint on the salinity of Enceladus' ocean, our purpose is to provide a broad physical picture of ocean circulation and heat transport on icy satellites forced by ice thickness variations and how these patterns depend on salinity. Further studies are needed to better understand and represent eddies, convection and boundary layer turbulence on icy moons and their impact on heat/tracer transport.

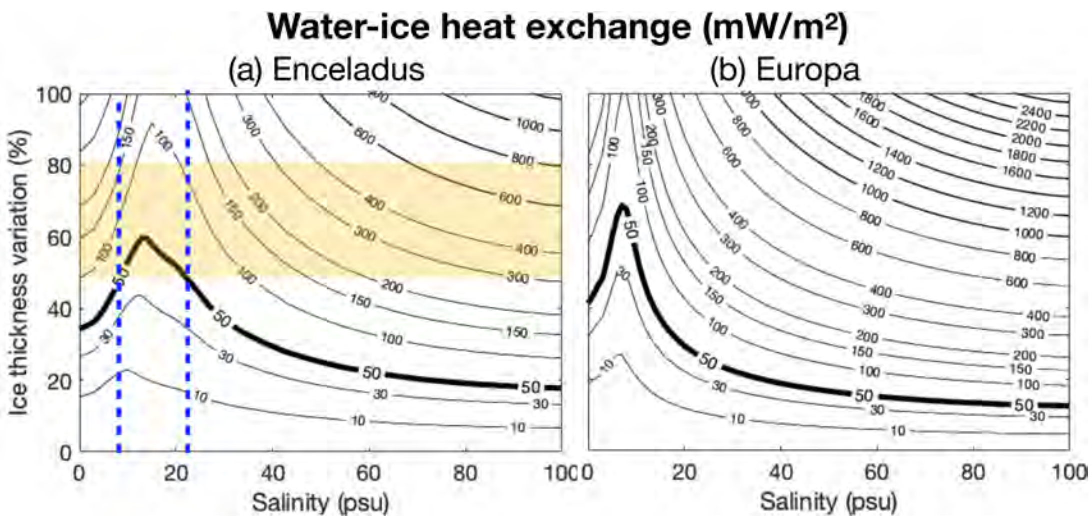

Figure 5: The water-ice heat exchange in equatorial regions for Enceladus (left) and Europa (right) predicted by our conceptual model (Eq.7) as a function of salinity and equator-to-pole percentage ice thickness variation (equatorial minus polar ice thickness divided by the mean). A degree-2 poleward-thinning structure is assumed and physical parameters are defined in Table 1. Parameter regimes that are consistent with observations are shaded in yellow: the ice shell of Enceladus is thought to have large thickness variations (*14–18*). The 50 mW/m^2 contour is highlighted by a thicker curve; heat exchange rates that exceed this are considered unphysical as the equatorial ice sheet of both Enceladus and Europa only allow $\sim$40 mW/m^2 or so of heat flux to conduct through. Our simplified model suggests that salinities on Enceladus and ice thickness variations for Europa lie in the region enclosed by the blue dashed lines. The most plausible ice-thickness variations and salinity on Enceladus thus lie in the yellow areas between the blue dashed lines.

4 Materials & Methods.

4.1 An overview of the General Circulation Model

Our simulations are carried out using the Massachusetts Institute of Technology OGCM (MITgcm (*63, 64*)) configured for application to icy moons. Our purpose is to 1) simulate the large-scale circulation and tracer transport driven by under-ice salinity gradients induced by patterns of freezing and melting, under-ice temperature gradients due to the pressure-dependence of the freezing point of water and bottom heat fluxes associated with tidal dissipation in the core, 2) diagnose the water-ice heat exchange rate and, 3) examine whether this heat exchange is consistent with the heat budget of the ice sheet, comprising heat loss due to conduction, tidal heating in the ice sheet, and heating due to latent heat release on freezing, as presented graphically in Fig. 1.

In our calculations the ice shell freezing/melting rate is derived from a model of ice flow (described below), based on observational inferences of ice shell thickness, prescribed and held constant: it is not allowed to respond to the heat/salinity exchange with the ocean underneath. To enable us to integrate our ocean model out to equilibrium on a 10,000 year timescales and to explore a wide range of parameters, we employ a zonally-symmetric configuration at relatively coarse resolution, and parameterize the diapycnal mixing, convection and baroclinic instability of small-scale turbulent processes that cannot be resolved. Each experiment is initialized from rest and a constant salinity distribution. The initial potential temperature at each latitude is set to be equal to the freezing point at the water-ice interface. The simulations are then launched for 10,000 years. By the end of 10,000 years of integration thermal equilibrium has been reached.

The model integrates the non-hydrostatic primitive equations for an incompressible fluid in height coordinates, including a full treatment of the Coriolis force in a deep fluid, as described in (*63, 64*). Such terms are typically neglected when simulating Earth's ocean because the ratio between the fluid depth and horizontal scale is small. Instead Enceladus' aspect ratio is order $40\text{km}/252\text{km}\sim 0.16$ and so not negligibly small. The size of each grid cell shrinks with depth due to spherical geometry and is accounted for by switching on the "deepAtmosphere" option of MITgcm. Since the depth of Enceladus' ocean is comparable to its radius, the variation of gravity with depth is significant. The vertical profile of gravity in the ocean and ice shell is given by, assuming a bulk density of $\rho_{\text{out}} = 1000$ kg/m^3:

$$g(z) = \frac{G\left[M - (4\pi/3)\rho_{\text{out}}(a^3 - (a-z)^3)\right]}{(a-z)^2}. \tag{8}$$

In the above equation, $G = 6.67 \times 10^{-11}$ N/m^2/kg^2 is the gravitational constant and $M = 1.08 \times 10^{20}$ kg and $a = 252$ km are the mass and radius of Enceladus.

Since it takes several tens of thousands of years for our solutions to reach equilibrium, we employ a moderate resolution of 2 degree (8.7 km) and run the model in a 2D, zonal-average configuration whilst retaining full treatment of Coriolis terms. By doing so, the zonal variations are omitted (the effects of 3D dynamics are to be explored in future studies). In the vertical direction, the 60 km ocean-ice layer is separated into 30 layers, each of which is 2 km deep. The ocean is encased by an ice shell with meridionally-varying thickness using MITgcm's "shelfice" and ice "boundary layer" module (*65*). We set the ice thickness H using the zonal average of the thickness map given by *Hemingway & Mittal 2019* (*18*), as shown by a solid curve in Fig. 1b, and assume hydrostacy (i.e., ice is floating freely on the water). We employ partial cells to better represent the ice topography: water is allowed to occupy a fraction of the height of a whole cell with an increment of 10%.

4.2 Parameterization of subgridscale processes

Key processes that are not explicitly resolved in our model are diapycnal mixing, convection and baroclinic instability. Here we review the parameterizations and mixing schemes used in our model to parameterize them. Sensitivity tests of our solutions when mixing parameters are varied about reference values are presented in the SM.

Vertical mixing of tracers and momentum

To account for the mixing of momentum, heat and salinity by unresolved turbulence, in our reference calculation we set the explicit horizontal/vertical diffusivity to 0.005 m^2/s. This is roughly 3 orders of magnitude greater than molecular diffusivity, but broadly consistent with dissipation rates suggested by *Rekier et al. 2019* for Enceladus (*21*), where both libration and tidal forcing are taken into account. According to (*21*), the tidal dissipation in the ocean is mostly induced by libration implying a global dissipation rate E of order 1 MW, but with considerable uncertainty. As reviewed by *Wunsch & Ferrari 2004* (*66*), this suggests a vertical diffusivity given by

$$\kappa_v = \frac{\Gamma\varepsilon}{\rho_0 N^2}, \tag{9}$$

where $\Gamma \sim 0.2$ is the efficiency at which dissipation of kinetic energy is available for production of potential energy. Here, $\varepsilon = E/V$ is the dissipation rate per volume, $V \approx 4\pi(a - H_0 - D/2)^2 D$ is the total volume of the ocean (H_0 and D are the mean thickness of the ice layer and ocean layer, and a is the moon's radius) and $\rho_0 \sim 1000$ kg/m^3 is the density of water. $N^2 = g(\partial \ln\rho/\partial z) \sim g(\Delta\rho/\rho_0)/D$ is the Brunt-Vaisala frequency, where g is the gravity constant. $\Delta\rho/\rho_0$ can be estimated from $\alpha_T \Delta T_f$, where α_T is the thermal expansion coefficient near the freezing point and ΔT_f is the freezing point difference between the underside of the equatorial and the north polar ice shell. Here we take $|\alpha_T| \sim 1 \times 10^{-5}$/K (corresponding to $S_0 = 27$ and $S_0 = 17$ psu), and $|\Delta T_f \sim 0.07|$K (a measure of the overall vertical temperature gradients in our default set of experiments). Substituting into Eq.9, yields $\kappa_v \sim 0.005$ m^2/s, which we choose to be the default horizontal and vertical diffusivity used in our experiments. The diffusivity for temperature and salinity are set to be the same, so that double diffusive effects are excluded. Uncertainties stem from both E and N^2 and show considerable spatial variability in our experients – see the discussion in (*21*). One might expect N^2 to be smaller (κ larger) in cases where temperature- and salinity-induced density gradients cancel one-another, and vice versa; the former scenario seems to be more plausible, a main conclusion of our study. It is for the reason that we set our default diffusivities to the above high values in all our reference experiments and explore the impact of lower diffusivities as sensitivity tests.

The horizontal and vertical viscosity ν_h, ν_v are set to 10 m^2/s. This value is the minimum needed to control grid-scale noise. In addition, to damp numerical noise induced by our use of stair-like ice topography, we employ a bi-harmonic hyperviscosity of 10^9 m^4/s and a bi-harmonic hyperdiffusivity of 5×10^7 m^4/s.

Despite use of these viscous and smoothing terms, the dominant balance in the momentum equation is between the Coriolis force and the pressure gradient force and so zonal currents on the large-scale remain in thermal wind balance, especially in the interior of the ocean. As shown by Fig. 6, the two-term balance in the thermal wind equation, $2\mathbf{\Omega} \cdot \nabla U = \partial b / a \partial \phi$ (see legend), are almost identical. Since thermal wind balance is a consequence of geostrophic and hydrostatic balance and the latter is always a good approximation on the large scale, geostrophic balance is indeed well satisfied.

Convection

Due to the coarse resolution of our model, convection cannot be resolved and must be parameterised. In regions that are convectively unstable, we set the diffusivity to a much larger value, 1 m^2/s, to represent the vertical mixing associated with convective overturns. Similar approaches are widely used to parameterize convection in coarse resolution ocean models (see, e.g. *Klinger and Marshall 1996* (*67*)) and belong to a family of convective adjustment schemes. This value is obtained based on the equilibrium top-to-bottom temperature gradient in a high-resolution Enceladus simulation (*68*), where we assume a salty ocean (40 psu) and enforce ~ 50 mW/m^2 of heat from the bottom. Scaling argument would lead to similar results. Accord-

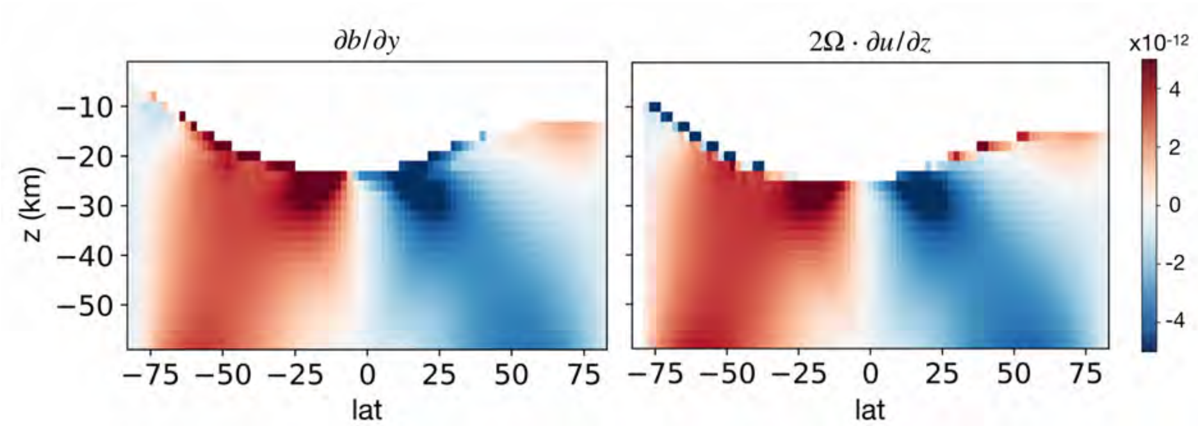

Figure 6: Thermal wind balance in the control simulation. Panels shows the two terms in the thermal wind balance, $2\mathbf{\Omega} \cdot \nabla U$ and $\partial b/a\partial\phi$, respectively. Here Ω is the rotation rate of the moon, U is the zonal flow speed, $b = -g(\rho - \rho_0)/\rho_0$ is buoyancy, a is the moon's radius and ϕ is latitude.

ing to *Jones and Marshall 1993* (*45*), the velocity in a rotation-dominated regime scales with $\sqrt{B/f}$, where B is the buoyancy flux and f is the Coriolis coefficient. Utilizing the fact that convective plumes/rolls should occupy the whole ocean depth D, a diffusivity can be estimated by multiplying the length scale and velocity scale together

$$\kappa_{\text{conv}} \sim \sqrt{B/f}D \sim 1\ m^2/s. \tag{10}$$

Here we have chosen B to be 10^{-13} m^3/s^2, which corresponds to the buoyancy flux produced by a 50 mW/m^2 bottom heat flux, or the buoyancy flux induced by a 1 km/My freezing rate, in an ocean with 40 psu salinity. This is 2 orders of magnitude lower than what is assumed in *Lobo et al. 2021* (*43*).

Our results are not found to be sensitive to the choice of κ_{conv} provided the associated diffusive time scale $D^2/\nu_{\text{conv}} \approx 0.5$ yr is much shorter than the advective time scale $M_{\text{half}}/\Psi \approx$ 2000 yrs (M_{half} is half of the total mass of the ocean and Ψ is the maximum meridional streamfunction in kg/s). It should be emphasized that, as noted above, away from boundary layers our solutions are close to geostrophic, hydrostatic and thermal wind balance and are not convectively unstable. However, convective heating from the bottom and/or salinization of water at the top can and do lead to convective instability which are mixed away diffusively.

Baroclinic instability

The large-scale currents set up in our model are in thermal wind balance with horizontal density gradients induced by under-ice temperature and salinity gradients. There is thus a store of available potential energy which will be tapped by baroclinic instability, a process which is not resolved in our model because of its zonally-symmetric configuration. Following an approach widely used in modeling Earth's ocean, we use the Gent-McWilliams (GM) scheme (*49, 69*) to parameterize the associated eddy-induced circulation and mixing of tracers along isopycnal surfaces. The key parameter that characterize the efficiency of the along-isopycnal mixing is the GM diffusivity κ_{GM}. To allow the along-isopycnal mixing rate to vary with the local stratification and isentrope slope, we adopt the κ_{GM} formula by *Visbeck et al. 1997* (*44*). The relevant parameters are listed in Table. 1.

Here, we will provide an rough estimate of κ_{GM} using the Visbeck formula:

$$\kappa_{\mathrm{GM}} = \alpha l^2 \frac{f}{\sqrt{\mathrm{Ri}}}, \tag{11}$$

where $\frac{f}{\sqrt{\mathrm{Ri}}}$ is proportional to the Eady growth rate, l is the width of the baroclinic zone, α=0.015 is a universal constant, f is the Coriolis parameter and $\mathrm{Ri} = N^2/U_z$ is the Richardson number. We estimate l using the Rhine's scale $\sqrt{U/\beta}$, where U is the zonal flow speed and β is the meridional gradient of the Coriolis parameter. Substituting $N^2 \sim 10^{-11}$ s^{-2}, $f \sim 10^{-4}$ s^{-1}, $U \sim 10^{-3}$ m, and $\beta \sim 10^{-10}$ s^{-1}m^{-1}, we find $\kappa_{\mathrm{GM}} \sim 0.3$ m^2/s. It is notable that this is 2-3 orders of magnitude smaller than the value used for Earth's ocean and those adopted by *Lobo et al. 2021* (*43*).

4.3 Equation of state and the freezing point of water

To make the dynamics as transparent as possible, we adopt a linear equation of state (EOS) to determine how density depends on temperature, salinity and pressure. The dependence of potential density ρ on potential temperature θ and salinity S is determined as follows:

$$\rho(\theta, S) = \rho_0 \left(1 - \alpha_T(\theta - \theta_0) + \beta_S(S - S_0)\right) \tag{12}$$

$$\rho_0 = \rho(\theta_0, S_0). \tag{13}$$

Here, $\rho_0,\ \theta_0$ and S_0 are the reference potential density, potential temperature and salinity. α_T and β_S, the thermal expansion coefficient and the haline contraction coefficient, are set to the first derivative of density with respect to potential temperature and salinity at the reference point using the Gibbs Seawater Toolbox (*24*). We carried out two test experiments (one with $S_0 = 10$ psu and the other with $S_0 = 20$ psu) using the full "MDJWF" equation of state (*70*) and obtained almost identical results. To explore a wide range of background salinity, S_0 is prescribed to values between 4 psu and 40 psu. θ_0 is set to be the freezing temperature at S_0 and $P_0 = 2.2 \times 10^6$ Pa (this is the pressure under a 20.8 km thick ice sheet on Enceladus).

The freezing point of water T_f is assumed to depend on local pressure P and salinity S as follows,

$$T_f(S, P) = c_0 + b_0 P + a_0 S, \tag{14}$$

where $a_0 = -0.0575$ K/psu, $b_0 = -7.61 \times 10^{-4}$ K/dbar and $c_0 = 0.0901$ degC. The pressure P can be calculated using hydrostatic balance $P = \rho_i g H$ ($\rho_i = 917$ kg/m^3 is the density of the ice and H is the ice thickness).

4.4 Boundary conditions

Our ocean model is forced by heat and salinity fluxes from the ice shell at the top as well as heat fluxes coming from below.

Diffusion of heat through the ice

Heat loss to space by heat conduction through the ice $\mathcal{H}_{\text{cond}}$ is represented using a 1D vertical heat conduction model,

$$\mathcal{H}_{\text{cond}} = \frac{\kappa_0}{H} \ln\left(\frac{T_f}{T_s}\right), \tag{15}$$

where H is the thickness of ice (solid curve in Fig. 1b), the surface temperature is T_s and the ice temperature at the water-ice interface is the local freezing point T_f (Eq. 14). We approximate the surface temperature T_s using radiative equilibrium based on the incoming solar radiation and obliquity ($\delta = 27°$) assuming an albedo of 0.81. The T_s profile is shown by the black solid curve in Fig.7. Typical heat losses averaged over the globe are $\mathcal{H}_{\text{cond}}$= 50 mW/m^2, broadly consistent with observations (*16*).

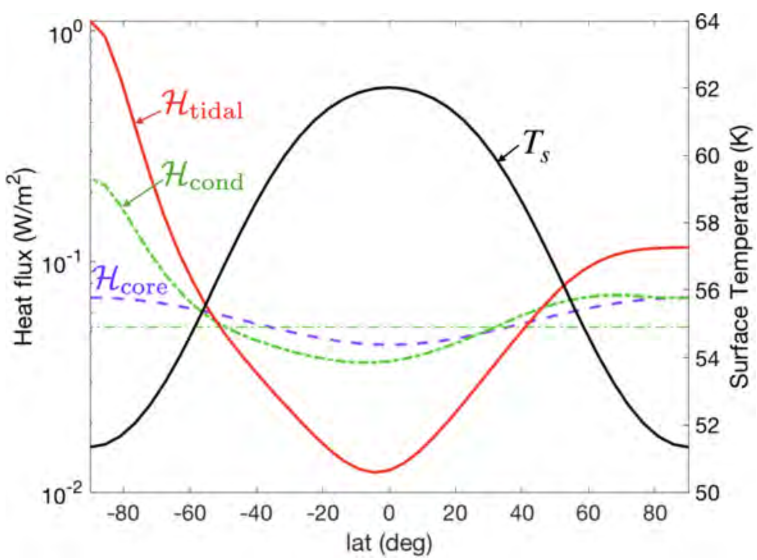

Figure 7: Meridional profiles of heat fluxes and surface temperature. Heat fluxes are plotted using colored curves, with a scale on the left. Conductive heat loss $\mathcal{H}_{\text{cond}}$ (Eq. 15) is shown by a thick green dash-dotted line which, in the global average, is balanced by heat generation in the silicate core $\mathcal{H}_{\text{core}}$ (purple dashed line, Eq. 16) and $\mathcal{H}_{\text{ice}}$ (red solid line, Eq. 26). All heat fluxes are normalized to have the same global mean value of $\mathcal{H}_{\text{cond}}$. The surface temperature T_s (black solid line, axis on the right) is set to be in radiative equilibrium with the solar radiation and is warmer at the equator.

Tidal heating in the core

Conductive heat loss is primarily balanced by tidal dissipation in the ice shell $\mathcal{H}_{\rm ice}$ and the core $\mathcal{H}_{\rm core}$ (dissipation in the ocean plays a negligible role) (*21, 23, 71, 72*). For each assumed heat partition between the shell and the core, we use the same meridional heating profiles for $\mathcal{H}_{\rm core}$ and $\mathcal{H}_{\rm ice}$ (see below). According to *Beuthe 2019* (*4*) and *Choblet et al. 2017* (*3*), the core dissipation $\mathcal{H}_{\rm core}$ peaks at the two poles. We obtain the meridional heat profile using Eq.60 in *Beuthe 2019* (*4*),

$$\mathcal{H}_{\rm core}(\phi) = \bar{\mathcal{H}}_{\rm core} \cdot (1.08449 + 0.252257\cos(2\phi) + 0.00599489\cos(4\phi)), \tag{16}$$

where ϕ denotes latitude and $\bar{\mathcal{H}}_{\rm core}$ is the global mean heat flux from the bottom. Since the global surface area shrinks going downward due to the spherical geometry, a factor of $(a-H)^2/(a-H-D)^2$ (H is ice thickness, D is ocean depth) needs to be considered when computing $\bar{\mathcal{H}}_{\rm core}$. The expression within the bracket is normalized for the globe, adjusted to take account of the fact that our model only covers 84S-84N. Using the above formula, the bottom heat flux is twice as strong over the poles than equator, as can be seen in Fig. 1d. We note that the heating profile here is highly idealized and does not have the localized heating stripes seen in *Choblet et al. 2017* (*3*) which arise from the interaction between the porous core and the fluid in the gaps.

Ice-ocean fluxes

The interaction between ocean and ice is simulated using MITgcm's "shelf-ice" package (*65, 73*). We turn on the "boundary layer" option to avoid possible numerical instabilities induced by an ocean layer which is too thin. The code is modified to account for a gravitational acceleration that is very different from that on earth, the temperature dependence of heat conductivity, and the meridional variation of tidal heating generated inside the ice shell and the ice surface temperature. In the description that follows, we begin by introducing the shelf-ice parameterization in a fully coupled ocean-ice system and then make simplifications that fit our goal here.

Following *Kang et al. 2020* (*68*), the heat budget involves three terms: the heat transmitted upward by ocean $\mathcal{H}_{\mathrm{ocn}}$, the heat loss through the ice shell due to heat conduction $\mathcal{H}_{\mathrm{cond}}$ (Eq.15), and the tidal heating generated inside the ice shell $\mathcal{H}_{\mathrm{ice}}$ (Eq.26). As elucidated in *Holland and Jenkins 1999* (*73*) and *Losch 2008* (*65*), the continuity of heat flux and salt flux through the "boundary layer" gives,

$$\mathcal{H}_{\mathrm{ocn}} - \mathcal{H}_{\mathrm{cond}} + \mathcal{H}_{\mathrm{ice}} = -L_f q - C_p(T_{\mathrm{ocn-top}} - T_b)q \tag{17}$$

$$\mathcal{F}_{\mathrm{ocn}} = -S_b q - (S_{\mathrm{ocn-top}} - S_b)q, \tag{18}$$

where $T_{\mathrm{ocn-top}}$ and $S_{\mathrm{ocn-top}}$ denote the temperature and salinity in the top grid of the ocean, S_b denotes the salinity in the "boundary layer", and q denotes the freezing rate in $kg/m^2/s$. $C_p = 4000$ J/kg/K is the heat capacity of the ocean, $L_f = 334000$ J/kg is the latent heat of fusion of ice.

$\mathcal{H}_{\mathrm{ocn}}$ and $\mathcal{F}_{\mathrm{ocn}}$ in Eq.17 can be written as

$$\begin{aligned}\mathcal{H}_{\mathrm{ocn}} &= C_p(\rho_0\gamma_T - q)(T_{\mathrm{ocn-top}} - T_b), & (19)\\ \mathcal{F}_{\mathrm{ocn}} &= (\rho_0\gamma_S - q)(S_{\mathrm{ocn-top}} - S_b) & (20)\end{aligned}$$

where $\gamma_T = \gamma_S = 10^{-5}$ m/s are the exchange coefficients for temperature and salinity, and T_b denotes the temperature in the "boundary layer". The terms associated with q are the heat/salinity change induced by the deviation of $T_{\mathrm{ocn-top}}$, $S_{\mathrm{ocn-top}}$ from that in the "boundary layer", where melting and freezing occur. $T_b = T_f(S_b, P)$, the freezing temperature at pressure P and salinity S_b (see Eq.14).

In a fully-coupled system, we would solve S_b and q from Eq. (17)-(20). When freezing occurs ($q > 0$), the salinity flux $\rho_{w0}\gamma_S(S_{\mathrm{ocn-top}} - S_b)$ is negative (downward). This leads to a positive tendency of salinity at the top of the model ocean, together with changes of temperature, thus:

$$\frac{dS_{\text{ocn-top}}}{dt} = \frac{-\mathcal{F}_{\text{ocn}}}{\rho_{w0}\delta z} = \frac{1}{\rho_{w0}\delta z}(\rho_{w0}\gamma_S - q)(S_b - S_{\text{ocn-top}}) = \frac{qS_{\text{ocn-top}}}{\rho_{w0}\delta z}, \tag{21}$$

$$\begin{aligned}\frac{dT_{\text{ocn-top}}}{dt} &= \frac{-\mathcal{H}_{\text{ocn}}}{C_p\rho_{w0}\delta z} = \frac{1}{\rho_{w0}\delta z}(\rho_{w0}\gamma_T - q)(T_b - T_{\text{ocn-top}}) \\ &= \frac{1}{C_p\rho_{w0}\delta z}\left[\mathcal{H}_{\text{ice}} - \mathcal{H}_{\text{cond}} + L_f q + C_p(T_{\text{ocn-top}} - T_b)q\right]\end{aligned} \tag{22}$$

where $\delta z = 2$ km is the thickness of the "boundary layer" at the ocean-ice interface.

It is worth pointing out that the top ocean grid is not at the freezing point exactly (it is close though), but this imaginary boundary layer is. When the ice is melting, this boundary layer will be fresher than the top ocean grid, to support a freshwater flux into the ocean. Having a relatively low salinity in the boundary layer means that the boundary layer temperature will be slightly higher given the dependence of freezing point on salinity (Eq. 14), which in turn allows heat to be transmitted toward the ocean, without requiring the ocean temperature to be below freezing.

If we allow the freezing/melting of ice and the ocean circulation to feedback onto one-another, the positive feedback between them renders it difficult to find consistent solutions. We therefore cut off this feedback loop by setting the freezing rate q to that which is required to sustain the prescribed ice sheet geometry (details can be found in the next subsection, ice flow model), whilst allowing a heating term to balance the heat budget (Eq.17). The amplitude of this heat imbalance can then be used to discriminate between different steady state solutions (Eq. 2). This also simplifies the calculation of the T/S tendencies of the upper-most ocean grid. The S tendency can be directly calculated from Eq. 21, and the T tendency approximated by:

$$\frac{dT_{\text{ocn-top}}}{dt} = \frac{1}{\delta z}(\gamma_T - q)(T_{\text{f,ocn-top}} - T_{\text{ocn-top}}), \tag{23}$$

replacing the boundary layer freezing temperature $T_b = T_f(S_b, P)$ in Eq. 22 with $T_{\text{f,ocn-top}} = T_f(S_{\text{ocn-top}}, P)$, the freezing temperature determined by the upmost ocean grid salinity and pressure. The difference between the S_b and $S_{\text{ocn-top}}$ can be estimated by $\mathcal{F}_{\text{ocn}}/(\rho_0\gamma_S) = qS_{\text{ocn-top}}/(\rho_0\gamma_S)$, according to Eq.20 and Eq.21, given that $|q| \lesssim 10^{-7}$ kg/m^2/s is orders of magnitude smaller than $\rho_0\gamma_S = 0.01$ kg/m^2/s. Even in the saltiest scenario we consider here, $|S_b - S_{\text{ocn-top}}|$ does not exceed 0.0004 psu, and the associated freezing point change is lower than 10^{-5}K. Readers interested in the formulation of a freely evolving ice-water system are referred to the method section of *Kang et al. 2021* (*68*) and *Losch 2008* (*65*).

In addition to the above conditions on temperature and salinity, the tangential velocity is relaxed back to zero at a rate of $\gamma_M = 10^{-3}$m/s at the upper and lower boundaries.

Ice flow model

We prescribe q using the divergence of the ice flow, assuming the ice sheet geometry is in equilibrium. We use an upside-down land ice sheet model following *Ashkenazy et al. 2018* (*41*). The ice flows down its thickness gradient, driven by the pressure gradient induced by the spatial variation of the ice top surface, somewhat like a second order diffusive process. At the top, the speed of the ice flow is negligible because the upper part of the shell is so cold and hence rigid; at the bottom, the vertical shear of the ice flow speed vanishes, as required by the assumption of zero tangential stress there. This is the opposite to that assumed in the land ice sheet model. In rough outline, we calculate the ice flow using the expression below obtained through repeated vertical integration of the force balance equation (the primary balance is between the vertical flow shear and the pressure gradient force), using the aforementioned boundary conditions to arrive at the following formula for ice transport $\mathcal{Q}$,

$$\begin{aligned}\mathcal{Q}(\phi) &= \mathcal{Q}_0 H^3(\partial_\phi H/a) \qquad (24)\\ \mathcal{Q}_0 &= \frac{2(\rho_0-\rho_i)g}{\eta_{\text{melt}}(\rho_0/\rho_i)\log^3(T_f/T_s)}\int_{T_s}^{T_f}\int_{T_s}^{T(z)} \exp\left[-\frac{E_a}{R_g T_f}\left(\frac{T_f}{T'}-1\right)\right]\log(T')\,\frac{dT'}{T'}\,\frac{dT}{T}.\end{aligned}$$

Here, ϕ denotes latitude, $a = 252$ km and $g = 0.113$ m/s^2 are the radius and surface gravity of Enceladus, T_s and T_f are the temperature at the ice surface and the water-ice interface (equal to local freezing point, Eq. 14), and $\rho_i = 917$ kg/m^3 and ρ_0 are the ice density and the reference water density (Eq. 12). $E_a = 59.4$ kJ/mol is the activation energy for diffusion creep, $R_g = 8.31$ J/K/mol is the gas constant and $\eta_{\rm melt}$ is the ice viscosity at the freezing point. The latter has considerable uncertainty (10^{13}-10^{15} Pa·s) (*39*) but we choose to set $\eta_{\rm melt} = 10^{14}$ Pa·s.

In steady state, the freezing rate q must equal the divergence of the ice transport thus:

$$q = -\frac{1}{a\cos\phi}\frac{\partial}{\partial\phi}(Q\cos\phi). \tag{25}$$

As shown by the dashed curve in Fig. 1b, ice melts in high latitudes and forms in low latitudes at a rate of a few kilometers every million years. A more detailed description of the ice flow model can be found in *Kang and Flierl 2020* (*50*) and *Ashkenazy et al. 2018* (*41*). Freezing and melting leads to changes in local salinity and thereby a buoyancy flux. At $S_0 = 30$ psu, the salinity-associated buoyancy flux is approximately $gq\beta_S S_0 \approx 10^{-13}$ m^2/s^3, which is 3-6 orders of magnitude smaller than the buoyancy flux used by *Lobo et al. 2021* (*43*).

4.5 Model of tidal dissipation in the ice shell

Enceladus's ice shell is periodically deformed by tidal forcing and the resulting strains in the ice sheet produce heat. We follow *Beuthe 2019* (*4*) to calculate the implied dissipation rate. Instead of repeating the whole derivation here, we only briefly summarize the procedure and present the final result. Unless otherwise stated, parameters are the same as assumed in *Kang & Flierl 2020* (*50*).

Tidal dissipation consists of three components (*4*): a membrane mode $\mathcal{H}_{\rm ice}^{\rm mem}$ due to the extension/compression and tangential shearing of the ice membrane, a mixed mode $\mathcal{H}_{\rm ice}^{mix}$ due to vertical shifting, and a bending mode $\mathcal{H}_{\rm ice}^{bend}$ induced by the vertical variation of compression/stretching. Following *Beuthe 2019* (*4*), we first assume the ice sheet to be completely flat. By solving the force balance equation, we obtain the auxiliary stress function F, which represents the horizontal displacements, and the vertical displacement w. The dissipation rate $\mathcal{H}_{\rm ice}^{\rm flat,x}$

(where $x = \{\mathrm{mem}, \mathrm{mix}, \mathrm{bend}\}$) can then be written as a quadratic form of F and w. In the calculation, the ice properties are derived assuming a globally-uniform surface temperature of 60K and a melting viscosity of 5×10^{13} Pa·s.

Ice thickness variations are accounted for by multiplying the membrane mode dissipation $\mathcal{H}_{\mathrm{ice}}^{\mathrm{flat,mem}}$, by a factor that depends on ice thickness. This makes sense because this is the only mode which is amplified in thin ice regions (see *Beuthe 2019* (*4*)). This results in the expression:

$$\mathcal{H}_{\mathrm{ice}} = (H/H_0)^{p_\alpha} \mathcal{H}_{\mathrm{ice}}^{\mathrm{flat,mem}} + \mathcal{H}_{\mathrm{ice}}^{\mathrm{flat,mix}} + \mathcal{H}_{\mathrm{ice}}^{\mathrm{flat,bend}}, \tag{26}$$

where H is the prescribed thickness of the ice shell as a function of latitude and H_0 is the global mean of H. Since thin ice regions deform more easily and produce more heat, p_α is negative. Because more heat is produced in the ice shell, the overall ice temperature rises, which, in turn, further increases the mobility of the ice and leads to more heat production (the rheology feedback).

Using reasonable parameters for Enceladus, $\mathcal{H}_{\mathrm{ice}}$ turns out to be at least an order of magnitude smaller than the heat loss rate $\mathcal{H}_{\mathrm{cond}}$. This is a universal flaw of present tidal dissipation models, and could be due to use of an over-simplified Maxwell rheology (*19, 75*). We therefore scale up $\mathcal{H}_{\mathrm{ice}}$ by a constant factor to obtain the desired magnitude. The tidal heating profile corresponding to $p_\alpha = -1.5$ is the red solid curve plotted in Fig. 7. In Fig. 4(b,e), we show the tidal heating profile for $p_\alpha = -1$ and $p_\alpha = -2$. The distribution of $\mathcal{H}_{\mathrm{ice}}$ is insensitive to the assumed ice viscosity, but the amplitude (before rescaling) could vary by a lot as indicated by previous studies (*74*).

References

1. F. Postberg, S. Kempf, J. Schmidt, N. Brilliantov, A. Beinsen, B. Abel, U. Buck and R. Srama, *Nature* **459**, 1098 (2009).

Symbol	Name	Definition/Value
	Enceladus parameters	
a	radius	252 km
δ	obliquity	27°
H	global mean ice thickness	20.8 km: ref (*18*)
D	global mean ocean depth	39.2 km: ref (*18*)
Ω	rotation rate	5.307×10^{-5} s^{-1}
g_0	surface gravity	0.113 m/s^2
$\bar{T}_s$	mean surface temperature	59K
	Europa parameters	
a	radius	1561 km
δ	obliquity	3.1°
H	global mean ice thickness	15 km: ref (*53*)
D	global mean ocean depth	85 km: ref (*53*)
Ω	rotation rate	2.05×10^{-5} s^{-1}
g_0	surface gravity	1.315 m/s^2
$\bar{T}_s$	mean surface temperature	110K
	Physical constants	
L_f	fusion energy of ice	334000 J/kg
C_p	heat capacity of water	4000 J/kg/K
$T_f(S,P)$	freezing point	Eq.14
ρ_i	density of ice	917 kg/m^3
ρ_w	density of the ocean	Eq.12
α, β	thermal expansion & saline contraction coeff.	using Gibbs Seawater Toolbox: ref (*24*)
κ_0	conductivity coeff. of ice	651 W/m: ref (*76*)
p_α	ice dissipation amplification factor	-2 $\sim$ -1
η_m	ice viscosity at freezing point	10^{14} Ps·s
	Default parameters in the ocean model	
$\nu_h,\ \nu_v$	horizontal/vertical viscosity	10 m^2/s
$\tilde{\nu}_h,\ \tilde{\nu}_v$	bi-harmonic hyperviscosity	10^9 m^4/s
$\kappa_h,\ \kappa_v$	horizontal/vertical diffusivity	0.005 m^2/s
$\alpha_{\rm GM}$	the universal constant used in GM scheme	0.015
$l_{\rm GM}$	the mixing length scale used in GM scheme	3 km
$S_{\rm GM}$	the maximum slope before clipping	0.2
$(\gamma_T,\ \gamma_S,\ \gamma_M)$	water-ice exchange coeff. for T, S & momentum	(10^{-5}, 10^{-5}, 10^{-3}) m/s
g	gravity in the ocean	Eq.8
P_0	reference pressure	$\rho_i g_0 H = 2.16\times10^6$ Pa
θ_0	reference potential temperature	$T_f(S_0, P_0)$
ρ_{w0}	reference density of ocean	Eq.13
$\mathcal{H}_{\rm cond}$	conductive heat loss through ice	Eq.15, Fig.7
$\mathcal{H}_{\rm ice}$	tidal heating produced in the ice	Eq.26, Fig.7
$\mathcal{H}_{\rm core}$	bottom heat flux powered by the core	Eq.16, Fig.7
A	surface albedo	0.81
T_s	surface temperature profile	Fig.7

Table 1: Model parameters used in our study.

2. P.C. Thomas, R. Tajeddine, M.S. Tiscareno, J.A. Burns, J. Joseph, T.J. Loredo, P. Helfenstein and C. Porco, *Icarus* **264**, 37 (2016).

3. G. Choblet, G. Tobie, C. Sotin, M. Běhounková, O. Čadek, F. Postberg and O. Souček, *Nature Astronomy* **1**, 841 (2017).

4. M. Beuthe, *Icarus* **332**, 66 (2019).

5. J. H. Waite, *et al.*, *Science* **311**, 1419 (2006).

6. H.W. Hsu, F. Postberg, Y. Sekine, T. Shibuya, S. Kempf, M. Horányi, A. Juhász, N. Altobelli, K. Suzuki, Y. Masaki and others, *Nature* **519**, 207 (2015).

7. H. J. Waite, C. R. Glein, R. S. Perryman, B. D. Teolis, B. A. Magee, G. Miller, J. Grimes, M. E. Perry, K. E. Miller, A. Bouquet, J. I. Lunine, T. Brockwell and S.J. Bolton, *Science* **356**, 155 (2017).

8. F. Postberg, S. Kempf, J. Schmidt, N. Brilliantov, A. Beinsen, B. Abel, U. Buck and R. Srama, *Nature* **558**, 564 (2018).

9. R. Taubner, P. Pappenreiter, J. Zwicker, D. Smrzka, C. Pruckner, P. Kolar, S. Bernacchi, A.H. Seifert, A. Krajete, W. Bach and others, *Nature communications* **9**, 1 (2018).

10. C. R. Glein, J. H. Waite, *Geophysical Research Letters* **47**, 591 (2020).

11. C. J. Hansen, L. Esposito, A.I.F. Stewart, J. Colwell, A. Hendrix, W. Pryor, D. Shemansky and R. West, *Science* **311**, 1422 (2006).

12. C. J. A. Howett, J. R. Spencer, J. Pearl, M. Segura, *Journal of Geophysical Research-Atmospheres* **116**, 189 (2011).

13. J. R. Spencer, C. J. A. Howett, A. Verbiscer, T. A. Hurford, M. Segura and D. C. Spencer, *European Planetary Science Congress* **8**, EPSC2013 (2013).

14. L. Iess, D. J. Stevenson, M. Parisi, D. Hemingway, R.A. Jacobson, J. I. Lunine, F. Nimmo, J. W. Armstrong, S. W. Asmar, M. Ducci and P. Tortora, *Science* **344**, 78 (2014).

15. M. Beuthe, A. Rivoldini, A. Trinh, *Geophysical Research Letters* **43**, 10,088 (2016).

16. R. Tajeddine, K. M. Soderlund, P. C. Thomas, P. Helfenstein, M. M. Hedman, J. A. Burns and P. M. Schenk, *Icarus* **295**, 46 (2017).

17. O. Čadek, O. Souček, M. Běhounková, G. Choblet, G. Tobie and J. Hron, *Icarus* **319**, 476 (2019).

18. D. J. Hemingway, T. Mittal, *Icarus* **332**, 111 (2019).

19. C. McCarthy, R. F. Cooper, *Earth and Planetary Science Letters* **443**, 185 (2016).

20. G. Tobie, A. Mocquet, C. Sotin, *Icarus* **177**, 534 (2005).

21. J. Rekier, A. Trinh, S. Triana, V. Dehant, *Journal of Geophysical Research: Planets* **124**, 2198 (2019).

22. K. M. Soderlund, K. Kalousová, J. J. Buffo, C. R. Glein, J. C. Goodman, G. Mitri, G. W. Patterson, F. Postberg, M. Rovira-Navarro, T. Rueckriemen and others, *Space Science Reviews* **216**, 1 (2020).

23. H. C. F. C. Hay, I. Matsuyama, *Icarus* **319**, 68 (2019).

24. T. J. McDougall, P. M. Barker, *SCOR/IAPSO WG* **127**, 1 (2011).

25. Y. Zeng, M. F. Jansen, *arXiv preprint arXiv:2101.10530* (2021).

26. J. Cullum, D. P. Stevens, M. M. Joshi, *Proceedings of the National Academy of Sciences* **113**, 4278 (2016).

27. B. Cael, R. Ferrari, *Geophysical Research Letters* **44**, 1886 (2017).

28. B. J. Travis, G. Schubert, *Icarus* **250**, 32 (2015).

29. O. Soucek, M. Behounkova, O. Cadek, J. Hron, G. Tobie and G. Choblet, *Icarus* **328**, 218 (2019).

30. G. Robuchon, G. Choblet, G. Tobie, O. Čadek, C. Sotin and O. Grasset, *Icarus* **207**, 959 (2010).

31. D. Shoji, H. Hussmann, K. Kurita, F. Sohl, *Icarus* **226**, 10 (2013).

32. M. Běhounková, G. Tobie, G. Choblet, O. Čadek, *Icarus* **226**, 898 (2013).

33. Y. Gevorgyan, G. Boué, C. Ragazzo, L. S. Ruiz, A. C. Correia, *Icarus* **343**, 113610 (2020).

34. M. Y. Zolotov, *Geophysical Research Letters* **34** (2007).

35. M. Y. Zolotov, F. Postberg, *LPI* p. 2496 (2014).

36. C. Glein, F. Postberg, S. Vance, *Enceladus and the icy moons of Saturn* **39** (2018).

37. A. P. Ingersoll, M. Nakajima, *Icarus* **272**, 319 (2016).

38. M. G. Fox-Powell, C. R. Cousins, *Journal of Geophysical Research: Planets* **126**, e2020JE006628 (2021).

39. G. Tobie, G. Choblet, C. Sotin, *J. Geophys. Res - Atmospheres* **108**, 219 (2003).

40. A. C. Barr, A. P. Showman, *Europa* (Univ. Arizona Press, 2009), pp. 405–430.

41. Y. Ashkenazy, R. Sayag, E. Tziperman, *Nature Astronomy* **2**, 43 (2018).

42. S. Bire, W. Kang, A. Ramadhan, J.-M. Campin, J. Marshall, *Journal of Geophysical Research: Planets* p. e2021JE007025 (2022).

43. A. H. Lobo, A. F. Thompson, S. D. Vance, S. Tharimena, *Nature Geoscience* pp. 1–5 (2021).

44. M. Visbeck, J. Marshall, T. Haine, M. Spall, *J. Phys. Oceanogr.* **27**, 381 (1997).

45. H. Jones, J. Marshall, *J. Phys. Oceanogr.* **23**, 1009 (1993).

46. A. Czaja, J. Marshall, *Journal of the atmospheric sciences* **63**, 1498 (2006).

47. H. Jeffreys, *Quarterly Journal of the Royal Meteorological Society* **51**, 347 (1925).

48. E. M. A. Chen, F. Nimmo, G. A. Glatzmaier, *Icarus* **229**, 11 (2014).

49. P. R. Gent, J. C. Mcwilliams, *Journal of Physical Oceanography* **20**, 150 (1990).

50. W. Kang, G. Flierl, *PNAS* **117**, 14764 (2020).

51. J. Marotzke, *Proc. Natl. Acad. Sci. U.S.A.* **97**, 1347 (2000).

52. J. Marshall, T. Radko, *J. Phys. Oceanogr.* **33**, 2341 (2003).

53. K. Hand, C. Chyba, *Icarus* **189**, 424 (2007).

54. M. Y. Zolotov, E. L. Shock, *Journal of Geophysical Research: Planets* **106**, 32815 (2001).

55. K. K. Khurana, M. G. Kivelson, K. P. Hand, C. T. Russell, *Robert. T. Pappalardo, William. B. McKinnon, and K. Khurana, Editors. Europa, University of Arizona Press, Tucson* pp. 572–586 (2009).

56. S. D. Vance, *et al.*, *arXiv preprint arXiv:2002.01636* (2020).

57. S. M. Howell, *The Planetary Science Journal* **2**, 129 (2021).

58. R. S. Park, B. Bills, B. B. Buffington, W. M. Folkner, A. S. Konopliv, T. J. Martin-Mur, N. Mastrodemos, T. P. McElrath, J. E. Riedel and M. M. Watkins, *Planetary and Space Science* **112**, 10 (2015).

59. M. Zannoni, D. Hemingway, L. G. Casajus, P. Tortora, *Icarus* p. 113713 (2020).

60. D. Durante, D. Hemingway, P. Racioppa, L. Iess, D. Stevenson, *Icarus* **326**, 123 (2019).

61. F. Nimmo, B. Bills, *Icarus* **208**, 896 (2010).

62. S. D. Vance, B. G. Bills, C. J. Cochrane, K. M. Soderlund, N. Gómez-Pérez, M. J. Styczynski, C. Paty, *arXiv preprint arXiv:2002.01636* (2020).

63. MITgcm-group, MITgcm User Manual, *Online documentation*, MIT/EAPS, Cambridge, MA 02139, USA (2010). http://mitgcm.org/public/r2_manual/latest/online_documents/manual.html.

64. J. Marshall, A. Adcroft, C. Hill, L. Perelman, C. Heisey, *J. Geophys. Res.* **102**, 5,753 (1997).

65. M. Losch, *J. Geophys. Res.* **113**, 10.1029/2007JC004368 (2008).

66. C. Wunsch, R. Ferrari, *Ann. Rev. Fluid Mech.* **36**, 281 (2004).

67. B. A. Klinger, J. Marshall, U. Send, *Journal of Geophysical Research: Oceans* **101**, 18175 (1996).

68. W. Kang, S. Bire, J-M Campin,C. Sotin, C. German, A. Thurnherr and J. Marshall, *arXiv preprint arXiv:2008.03764* (2020).

69. M. H. Redi, *J. Phys. Oceanogr.* **12**, 1154 (1982).

70. T. J. McDougall, D. R. Jackett, D. G. Wright, R. Feistel, *Journal of Atmospheric and Oceanic Technology* **20**, 730 (2003).

71. Chen, E M A, Nimmo, F, *Icarus* **214**, 779 (2011).

72. M. Beuthe, *Icarus* **280**, 278 (2016).

73. D. M. Holland, A. Jenkins, *J. Phys. Oceanogr.* **29**, 1787 (1999).

74. M. Beuthe, *Icarus* **302**, 145 (2018).

75. J. P. Renaud, W. G. Henning, *Astrophysical Journal* **857**, 98 (2018).

76. V. Petrenko, R. Whitworth, *Physics of Ice* (OUP Oxford, 1999).

77. J. Smagorinsky, *Mon. Weath. Rev.* **91**, 99 (1963).

78. K. M. Soderlund, *Geophysical Research Letters* **46**, 8700 (2019).

79. Y. Ashkenazy, E. Tziperman, *arXiv preprint arXiv:2006.02242* (2020).

Acknowledgments

This work was carried out in the Department of Earth, Atmospheric and Planetary Science (EAPS) in MIT. WK and TM acknowledges support as a Lorenz/Crosby Fellow supported by endowed funds in EAPS. SB, JC and JM acknowledge part-support from NASA Astrobiology Grant 80NSSC19K1427 Exploring Ocean Worlds. We thank Mikael Beuthe and Malte Jansen for advice and discussions.

Data and Materials Availability

All data needed to evaluate the conclusions in the paper are present in the paper and/or the Supplementary Materials.

Supplementary materials

Exploring the sensitivity of ocean model solutions to parameters

Figs. S1 to S11

Refs. 77-79